<div align="center">

SUPPORTING INFORMATION

Dehydra-Decyclization of 2-Methyltetrahydrofuran to Pentadienes on Boron-Containing Zeolites

</div>

<div align="center">

Gaurav Kumar[‡], Dongxia Liu[†], Dandan Xu[β], Limin Ren[‡,δ],
Michael Tsapatsis[ξ,g,*], Paul J. Dauenhauer[‡,η,*]

</div>

[‡] Department of Chemical Engineering and Materials Science, University of Minnesota, 421 Washington Ave. SE, Minneapolis, MN 55455, USA

[†] Department of Chemical and Biomolecular Engineering, University of Maryland, College Park, MD, 20742, USA

[β] Department of Chemical Engineering, University of Massachusetts Amherst, 686 N. Pleasant Street, Amherst, MA 01003, USA

[δ] Zhang Dayu school of chemistry, Dalian university of technology, No. 2 Linggong Road, Dalian, China, 116024

[ξ] Department of Chemical and Biomolecular Engineering & Institute for NanoBioTechnology, Johns Hopkins University, 3400 N. Charles Street, Baltimore, MD 21218, USA

[g] Johns Hopkins University, Applied Physics Laboratory, 11100 Johns Hopkins Road, Laurel, MB 20723, USA

[η] Center for Sustainable Polymers, University of Minnesota, 207 Pleasant St. SE, Minneapolis, MN 55455, USA

*Corresponding Authors: hauer@umn.edu, tsapatsis@jhu.edu

INDEX

S1. Synthesis and characterization results for all synthesized samples
S1.1 Synthesis of zeolites

MCM-22

Briefly, 1.32 g NaOH pellets were dissolved in 233.06 g deionized water (18.2 MΩ). Thereafter 1.37 g $NaAlO_2$ was added till full dissolution, followed by the addition of 14.34 g hexamethyleneimine(HMI). 17.68 g of fumed silica (Cab-o-sil M5) was added under stirring conditions, and mixture was stirred till a homogeneous gel was obtained. This gel with the chemical composition SiO_2: 0.112 NaOH: 0.493 HMI: 0.057 $NaAlO_2$: 44.04 H_2O was treated hydrothermally at 408 K for eleven days under rotation. Upon removal, ion exchange was performed by preparing 5% w/w mixture of Na-form of the prepared sample with 1.0 M NH_4NO_3 solution and keeping the solution under stirring conditions at 343 K for 12 hours. This material is the Al-MWW precursor (denoted as Al-MWW(P)). Calcination of this precursor lead to MCM-22.

MCM-36

For the synthesis of MCM-36, a wet cake of Al-MWW (P) (20 wt% solids) was swollen at room temperature under high pH conditions (pH~14) followed by pillaring of the swollen materials with TEOS. In the swelling process, typically, 9 g of wet cake of Al-MWW(P) was mixed with 35 g of an aqueous solution of 29 wt% CTAB and 11 g of an aqueous solution of 40 wt% TPAOH. The mixture was allowed to stir for 16 h at ambient temperature, and then the particles were recovered by repeated cycles of centrifugation and water washing (600 s centrifugation at 10000 rpm, and re-dispersion in fresh water). The swollen material was then dried at 343 K overnight. The pillaring process was conducted by mixing 5 g of swollen Al-MWW(P) powder with 25 g of TEOS, stirring for 24 h at 351 K under argon atmosphere, then filtering and drying at ambient temperature. A 1.0 g sample of the resulting solid was hydrolyzed with 10 g of water (pH ~ 8, controlled with NaOH) for 6 h at 313 K, then filtered, dried at 300 K to produce pillared MWW (MCM-36). After calcination (as described in the main text), successful swelling and pillaring of Al-MWW (P) was confirmed by the presence of (001) peak in the XRD patterns **(Figure S1B)**, as well the visible stacking of layers in the scanning TEM micrographs (**Figure S1H**).

B-MWW

8.04 g of boric acid was dissolved into 68.4 g deionized water (18.2 MΩ). After complete dissolution, 23.84 g of piperidine was added, and the mixture was stirred for 30 minutes. 12.0 g of fumed silica (Cab-o-sil M5) was then added to the above solution. A vortex shaker was used to mix the gel for at least 20 minutes prior to setting up magnetic stirring overnight, and the gel appeared translucent milky after vortex mixing. After

stirring overnight, this gel with chemical composition SiO_2: 1.4 PI: 19 H_2O:0.65 H_3BO_3 was transferred to autoclaves and hydrothermally treated in a rotation oven at 443 K for seven days.

B-MFI

1.13 g of anhydrous borax was dissolved into 29.0 g of deionized water (18.2 MΩ). 4.5 g TPAOH and 4.5 g solid NaOH were added, and the solution was stirred for 30 minutes. Then, 2.71 g of fumed silica (Cab-o-Sil M5) was added to the solution, and the gel was stirred overnight. The gel with a chemical composition SiO_2: 0.49 TPAOH: 2.5 NaOH: 36 H_2O: 0.13 $Na_2B_4O_7$ was then transferred to autoclaves and hydrothermally treated in a static oven at 453 K for five days. Upon removal, ion exchange was performed by preparing 5% w/w mixture of Na-form of the prepared sample with 1.0 M NH_4NO_3 solution and keeping the solution under stirring conditions at 343 K for 12 hours.

B-BEA

0.54 g of boric acid was dissolved into 68.5 g deionized water (18.2 MΩ) and 22.83 g of TEAOH. The solution was stirred for 30 minutes. Then 24.03 g of fumed silica (Cab-o-sil M5) and 1.17 Si-BEA seeds (synthesized using procedures listed elsewhere[1]) were added to the above solution. After stirring for two hours, the gel with chemical composition SiO_2: 0.385 TEAOH: 14 H_2O: 0.067 H_3BO_3 was transferred to autoclaves and hydrothermally treated in a static oven at 423 K for four days.

Following hydrothermal treatment for B-BEA and B-MWW, and ion-exchange for B-MFI and MCM-22, all samples were separated and fully washed and centrifuged to pH ~ 9.0 followed by drying at 343 K overnight. These were then calcined using procedures reported in the main text.

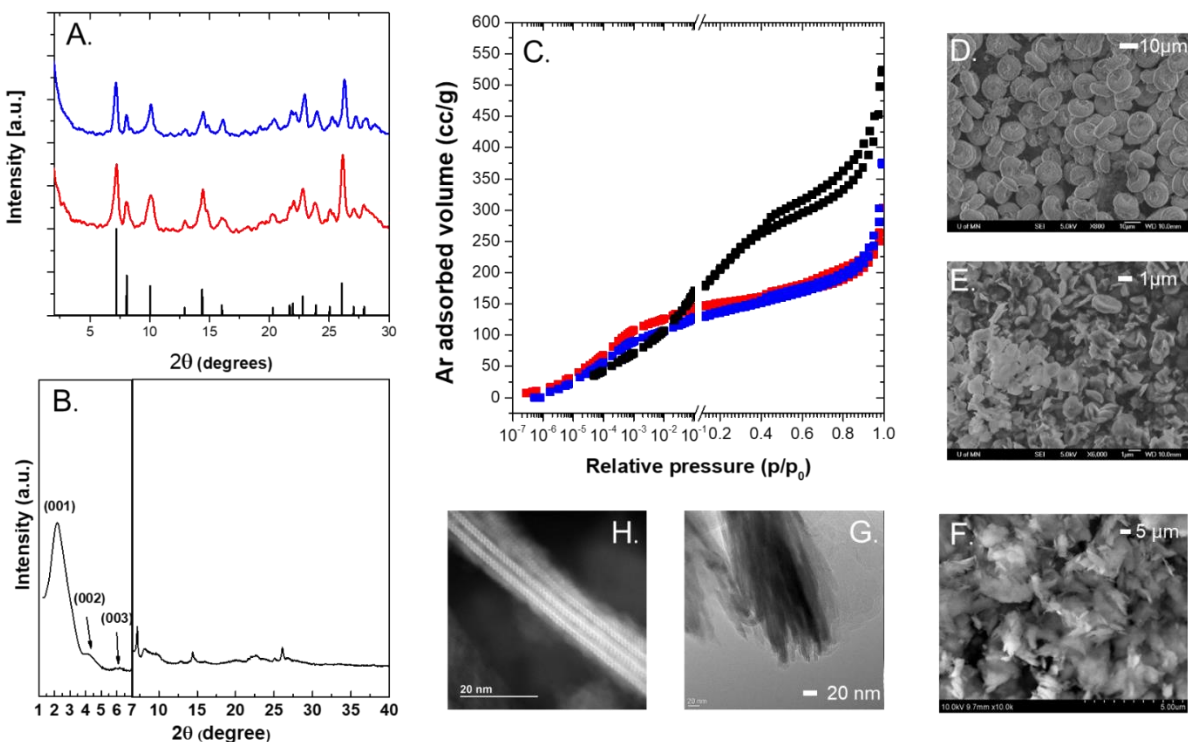**S1.2 Characterization results for all zeolites with MWW topology**

Figure S1. (A) PXRD patterns for B-MWW, and MCM-22 compared with *(bottom)* MWW XRD pattern from International Zeolite Association (IZA)[2] ; **(B)** PXRD pattern for MCM-36; **(C)** Ar adsorption-desorption isotherms for B-MWW(■), MCM-22 (■) and MCM-36 (■); **(D)** SEM micrograph for B-MWW; **(E)** SEM micrograph for MCM-22; **(F)** SEM micrograph of MCM-36; **(G)** TEM micrograph of MCM-22 and **(H)** STEM image of MCM-36. Note that the presence of 001 peak **(Figure S1B)** indicates successful pillaring of MCM-22 to MCM-36 (long range order is preserved, and stacked layers are also visible in STEM image in **Figure S1H**

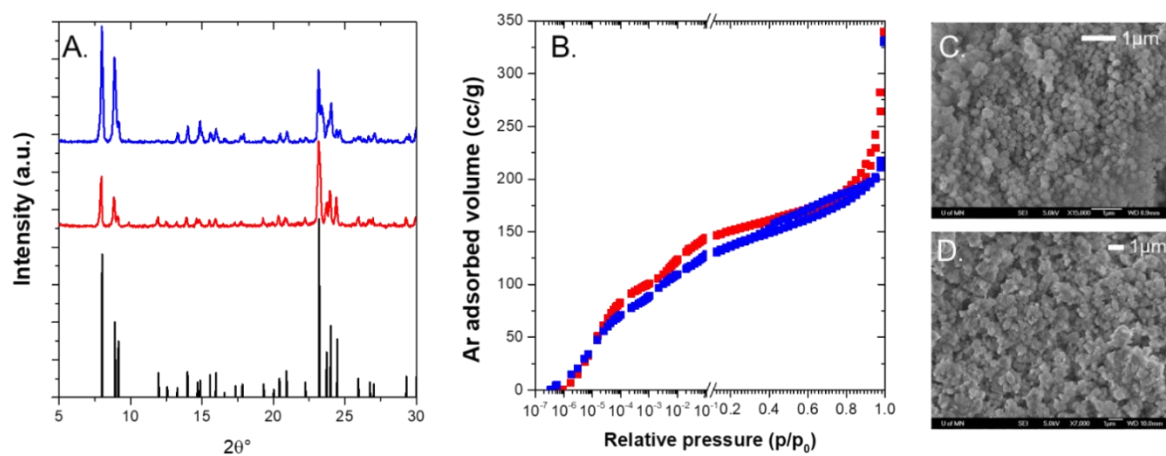**S1.3 Characterization results for all zeolites with MFI topology**

Figure S2. (A) PXRD patterns for B-MFI, and ZSM-5 compared with *(bottom)* MFI XRD pattern from International Zeolite Association (IZA);[2] **(B)** Ar adsorption-desorption isotherms for B-MFI (■) and ZSM-5 (■); **(C)** SEM micrograph for B-MFI; **(D)** SEM micrograph for ZSM-5.

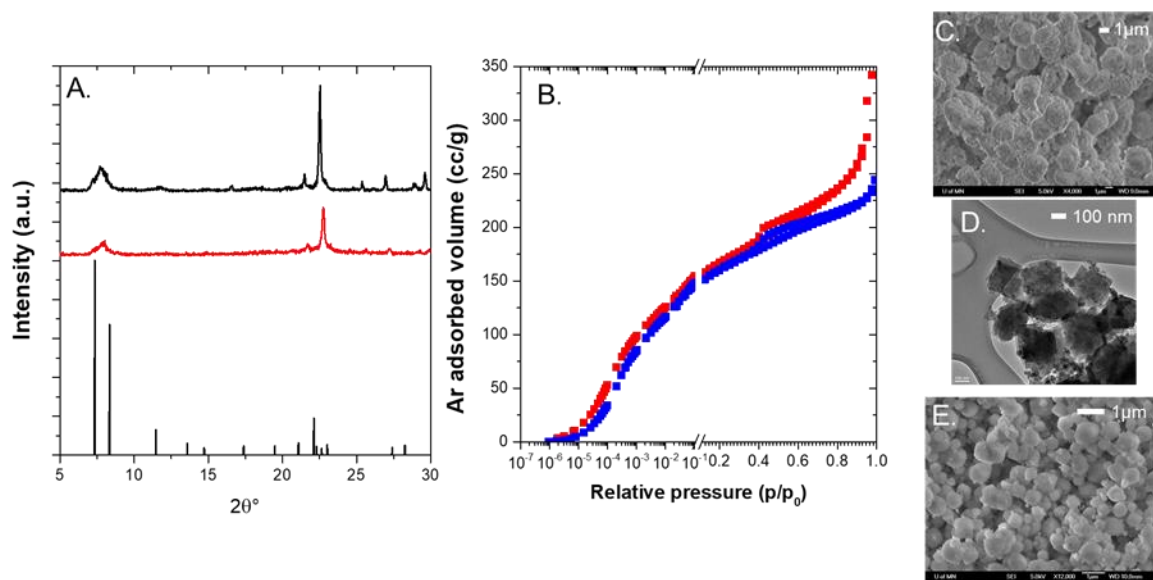**S1.4 Characterization results for all zeolites with BEA topology**

Figure S3. (A) PXRD patterns for B-BEA, and Al-BEA compared with *(bottom)* BEA XRD pattern from International Zeolite Association (IZA);[2] **(B)** Ar adsorption-desorption isotherms for B-BEA (■) and Al-BEA (■); **(C)** SEM micrograph for B-BEA; **(D)** TEM micrograph for B-BEA; **(E)** SEM micrograph of Al-BEA.

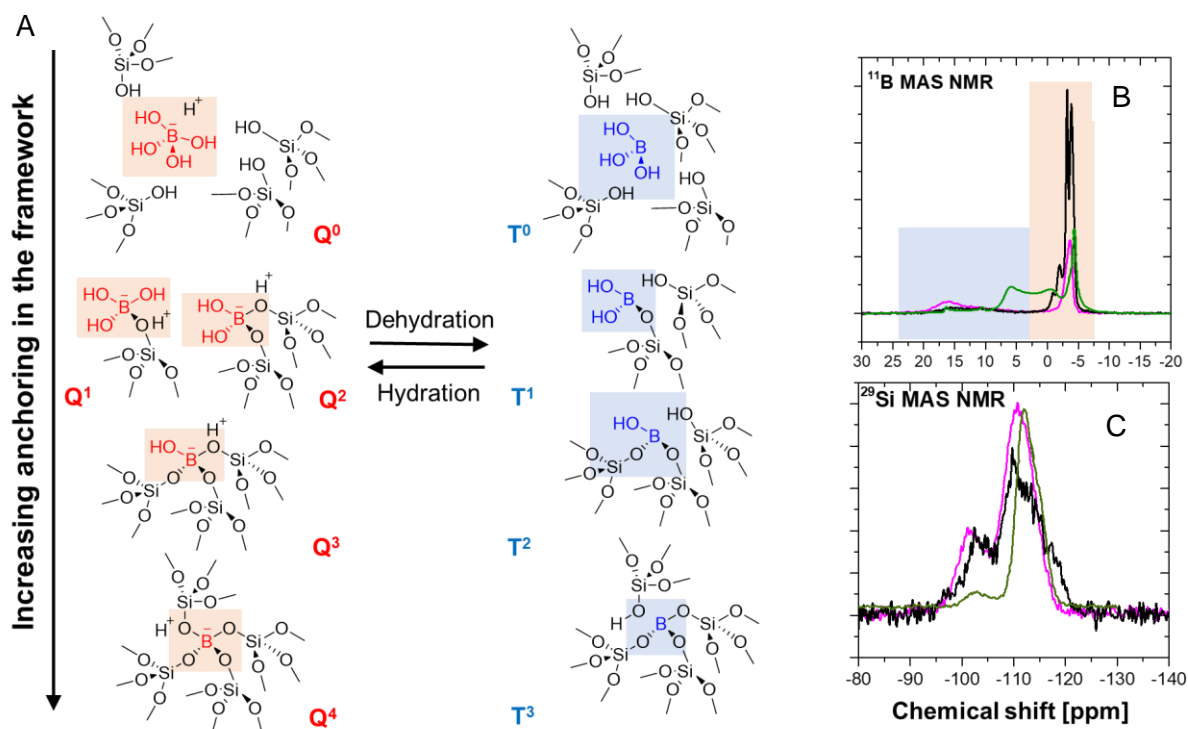## S1.5 Ex-situ characterization of boron and silicon environments in borosilicates

Figure S4. (A) Trigonal and tetrahedral boron environments in borosilicates; **(B)** ^{11}B MAS NMR spectra; and **(C)** ^{29}Si MAS NMR spectra of B-MWW, B-BEA, and B-MFI.

Numerous reports on the silicon states in aluminosilicates as well as borosilicates exist and are not discussed in detail here for brevity. Briefly, the occupancy of Si in these frameworks is either in form of $Si(OSi)_4$ linkages (represented as Q^4 by ^{29}Si-NMR), or as defect silanol nests $Si(OSi)_3OH$ (represented as Q^3). Q^4 shows a chemical shift of ~ -110 ppm whereas Q^3 shows a shift of ~ -100 ppm in ^{29}Si MAS NMR spectra. Both signals were found present in all the synthesized borosilicate samples **(Figure S4C)**. As hydrolysis of B-O-Si bonds leads to the formation of silanol nests, a relatively weak Q^3 signal in all samples indicated that most B-O-Si bonds were intact.[3,4] Previous reports have further highlighted that boron coordination is mostly trigonal in dehydrated samples, and it undergoes a change to tetrahedral state upon rehydration.[5,6] However, it is also possible that upon addition of excess water, trigonal (three-coordinated) B is hydrolyzed to a defect terminal B-OH linkage which can be completely extracted from the framework.[7] The broad range for tetrahedral B chemical shifts are in the range of -5 to 0 ppm, while different trigonal sites show a chemical shift in the range ~ 3 to 18 ppm in ^{11}B MAS NMR spectra, depending on the anchoring of B in the framework.[5,6,8,9] **Figure S4A** depicts an exhaustive list of boron environments in borosilicates. It can be seen that trigonal sites T^0, T^2, T^3, can transform into tetrahedral sites (Q^0, Q^3, Q^4), respectively, on the addition of water, and this change is reversible upon dehydration. Such transformations can also take place upon interaction of trigonal B sites with bases like pyridine and ammonia.[8,10] Signals corresponding

to both trigonal and tetrahedral B environments were present in the ^{11}B MAS NMR spectra of all three borosilicates considered in this work **(Figure S4B)**. Interestingly, B-MWW showed a multiplet for tetrahedral B. Generally, the different chemical environments of boron atoms at *T*-positions in zeolite frameworks only have a minor influence on chemical shifts in ^{11}B MAS NMR spectra,[5] and multiplets in this region are attributed to the presence of non-identical crystallographic distinct *T*-sites in frameworks including B-MWW,[11] B-RUB-1[12] and B-FER.[9] MWW has eight distinct *T*-sites, and the result indicates that B-MWW preserves long-range order of B in these distinct tetrahedral sites resolvable by ^{11}B NMR. It is also possible that B-MWW has higher B content than the other two borosilicates, and hence the distinct local environments are resolved in it. An accurate siting of B at these distinct sites, while possible using site multiplicities and previously reported relative stability of B in these distinct sites,[11] is challenging using 1-D NMR experiments alone. At each crystallographically distinct *T*-position, B can be sited in any of Q^0-Q^4 environments, making it difficult to accurately predict their NMR shifts, and hence an accurate assignment of the multiplet lies outside the scope of this work.

S2. Assessment of transport limitation during kinetic measurements

Mears' Criterion was used to estimate the existence of any external mass transfer calculations when measuring reaction rates. This was done for the catalyst exhibiting the highest mass-normalized rates (Al-BEA) at the highest temperature (513 K). It can be safely assumed that the less active catalysts (per mass basis) will not be external transport-limited provided this limiting case doesn't show these artifacts at identical reaction conditions. External mass transfer limitations can be neglected if the following inequality is satisfied

$$\frac{r_{obs}\rho_b R n}{k_c C_b} < 0.15 \tag{S.1}$$

Where r_{obs} is the observed rate of reaction in mol $kgcat^{-1}$ s^{-1}, ρ_b is the catalyst bed density in kg m^{-3} (ρ_b = (1-ϕ)ρ_c where ϕ is the bed void fraction and ρ_c is the density of the catalyst, reported as 1000 kg m^{-3}), R is the catalyst aggregate size in m, n is the reactant reaction rate order, k_c is the external mass transfer coefficient in m s^{-1}, and C_b is the reactant bulk concentration in mol m^{-3}.

Table S1. Tabulation of parameters for the calculation of Mears' Criteria for 2-MTHF dehydra-decyclization on Al-BEA (Si/Al 12.5) at 513 K

Parameter	Value
r_{obs} (mol $kgcat^{-1}$ s^{-1})	4.34 x 10^{-3}
ρ_b (kg_{cat} m^{-3})	700 (ρ_c = 1000, assumed ϕ = 0.3)
R (m)	3.75x10^{-4} (average mesh size of 250-500 μm)
k_c (m s^{-1})^a	0.102
C_b (mol m^{-3})	0.31 (10.5 torr 2-MTHF; total pressure 787.6 torr)
n	0
Mears' Criterion (Mass)	**0 (3.6 x 10^{-2} if assumed n = 1)**

^{a} Estimated assuming Sh (Sherwood Number) = $k_c(2R)/D$ = 2 + 0.6 $Re^{1/2}Sc^{1/3}$; Re (Reynolds Number) = $\rho U(2R)/\mu$ and Sc (Schmidt number) = $\mu/\rho D$, where ρ = bulk gas density (Assumed to be He at 513 K, ρ = 0.15 kg m^{-3}), U = superficial velocity (total volumetric flow rate (1 cm^3 s^{-1}); tube diameter (2R) = 4 x10^{-3} m: U = 7.95x10^{-2} m s^{-1}), and μ = gas viscosity (estimated as He viscosity at 513 K = 2.85 x 10^{-5} Pa s). D is gas phase diffusivity, estimated using Chapman-Enskog theory of diffusivity for 2-MTHF in He at 513 K =2.47 x 10^{-4} m^2 s^{-1}).

The Mears criterion parameter show the reported rates are not corrupted by external mass transfer limitations.

Internal mass transfer limitations were evaluated by using the Weisz-Prater criterion **(Eq S.2)** for the highest temperature on all the six catalysts.

$$C_{WP} = \eta \phi^2 = \frac{r_{obs}\rho_c R^2}{D_e C_{As}} \tag{S.2}$$

where η is the dimensionless effectiveness factor, ϕ^2 is the dimensionless Thiele modulus, D_e is the effective diffusivity in m^2s^{-1} ($D_e = D\varepsilon\delta/\tau$, where ε is the porosity, δ is the constrictivity, and τ is the tortuosity, assumed to be average values of 0.35, 0.8, and 6, respectively), ρ_c is the particle density of the catalyst (assumed 1000 kg/m^3) and C_{As} is the reactant surface concentration in mol m^{-3} (Mears' criterion showed that there were no external mass transfer limitations, and hence we assume $C_{As} = C_b$). The upper limit of $\eta\varphi^2$ to safely assume that reaction is not diffusion limited is typically taken to be ~0.3.

The evaluation of D_e requires sorption experiments with framework dependent probe molecules, and we instead adopted an alternative method for these internal transport calculations. A prior study by Ruthven and co-workers has measured the effective diffusivity of 2-methyl cyclopentane (2-MCP) in silicalite-1,[13] which was assumed to be a surrogate for 2-MTHF given their similar sizes and chemical structures. Setting the value of Weisz-Prater parameter to 0.3 at the experimentally observed rates, the lower limit of D_e ($D_{e,min}$) which would still ensure the rates to be in kinetic regime was calculated for each catalyst, and compared with the effective diffusivity of 2-MCP ($D_{e,2\text{-MCP, actual}}$) in MFI micropores at the same temperature. Conclusions drawn from these calculations were different for the different frameworks.

a) MFI: If $D_{e,min} < D_{e,2\text{-MCP, actual}}$, the rates are strictly in kinetic regime and internal transport limitations are absent. If $D_{e,min} > D_{e,2\text{-MCP, actual}}$, internal transport limitations exist.

b) MWW: If $D_{e,min} > D_{e,2\text{-MCP, actual}}$, we can conclude that we are diffusion limited in the sinusoidal 10-MR channels of MWW (as they are smaller than MFI). However, the result is inconclusive if the opposite is true ($D_{e,min} < D_{e,2\text{-MCP, actual}}$). In short, the criteria can only confirm if we are diffusion-limited but not sufficient to prove if we are reaction-limited or not.

c) BEA: If $D_{e,min} < D_{e,2\text{-MCP, actual}}$, we can certainly say that we are not diffusion-limited in BEA (given BEA has larger micropores than MFI). However, the test remains inconclusive in the case $D_{e,min} > D_{e,2\text{-MCP, actual}}$. In short, the criteria can only confirm if we are reaction-limited but not sufficient to prove if we are diffusion-limited or not.

The results of this calculation for B-MFI and ZSM-5 are shown in **Figure S5 (A-B)**. Since $D_{e,min} < D_{e,2\text{-MCP, actual}}$ for both B-MFI and ZSM-5 at the three highest temperatures of kinetic investigation, these data are in kinetic regime. The rates (per mass) for Al-BEA are within ~2x of ZSM-5 while the difference in $D_{e,min}$ and $D_{e,2\text{-MCP}}$ were almost an order of magnitude, and a similar analysis shows absence of internal transport limitations in Al-BEA as well. Similarly, B-BEA is significantly less active than B-MFI, and one can safely assume that absence of internal transport limitations in B-MFI implies that the data for B-BEA are also in kinetic regime.

The situation changes, however, in the case of both MWW catalysts. We note that the correct length scale to be used in the Thiele modulus formalism should not be the thickness of the platelet-shaped crystallites **(Figure S1 D-F)** but rather their diameter; the transport through external surface pockets to the crystallite is inhibited by 6-MR constrictions, and only happens through the sinusoidal 10-MR channels (which are somewhat smaller than MFI). The results of the calculations for MWW catalysts are shown in **Figure S5 (C-D)**. On MCM-22, $D_{e,min} \approx D_{e,\text{2-MCP, actual}}$, and we cannot rule out the presence of diffusional limitations. While data for only the highest three reaction temperatures is shown, this was also found to be the case at low temperatures (453 K). Therefore, even under reaction conditions used for DTBP titration experiments, the measurements were not strictly in kinetic regime. Similarly, for B-MWW, $D_{e,min} > D_{e,\text{2-MCP, actual}}$ which means that the presence of internal transport artifacts certainly cannot be ruled out in the rate measurements. We therefore don't report activation barriers for the MWW catalysts as the rates are not strictly in the kinetic regime under the reaction conditions.
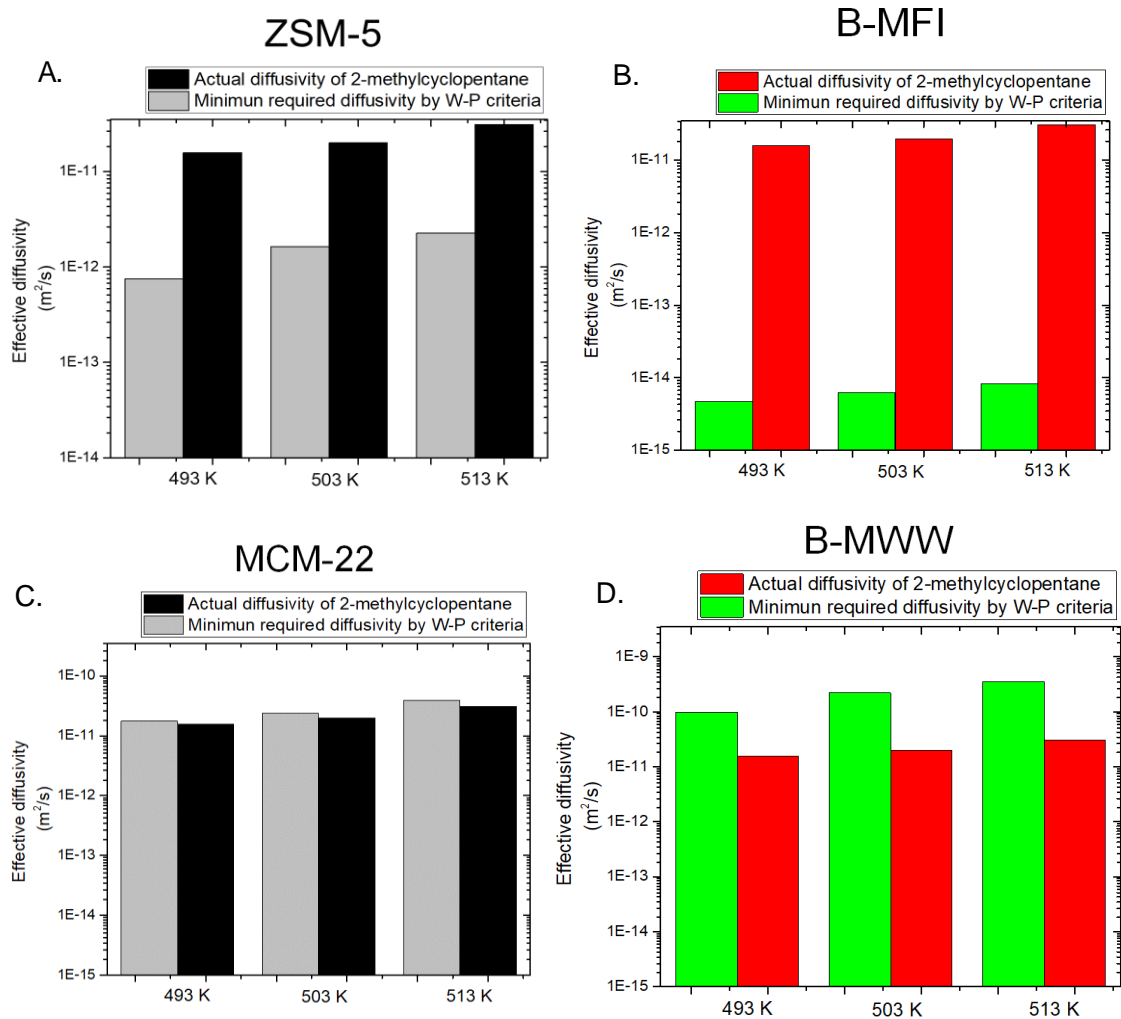
Figure S5. Comparison of $D_{e,min}$, and $D_{e,2\text{-MCP, actual}}$ under 2-MTHF reaction conditions for **(A)** ZSM-5, **(B)** B-MFI, **(C)** MCM-22, and **(D)** B-MWW.

S3. Catalytic performance of all zeolites for the dehydra-decyclization of 2-MTHF

While all mechanistic inquiries were sought under differential conditions, all zeolite samples were evaluated at different conversions to evaluate the product distributions and explore the range of 1,3-Pentadiene yields achievable. **Table S2** lists all the experiments conducted at relatively high temperatures, low 2-MTHF partial pressures, and low weight hourly space velocities to maximize conversions.

Table S2. Reaction conditions and obtained product selectivities to major products

Catalyst	T (K)	WHSV (h^{-1})	Conversion (%)	Carbon selectivity (%)			
				1,3-PD	(1,3+1,4)-PD	Butenes	C6+
B-MFI	608	0.89	35.2 (32.5)	63.5 (62.5)	89.3 (88.5)	3.5 (3.2)	1.5 (1.8)
	608	0.57	58.5	70.2	89.1	3.2	5.2
	658	0.21	93.3	83.2	91.2	3.5	5.6
	608	1.50	7.5	52.2	88.2	2.9	4.3
	608	0.45	47.7	71.1	89.9	3.1	5.1
ZSM-5	608	0.86	69.5	74.6	77.9	8.5	7.8
B-BEA	608	0.89	9.2 (8.1)	46.0 (45.2)	91.4 (90.5)	0.5 (0.4)	2.7 (2.4)
	658	0.16	44.9	53.3	87.8	1.5	5.2
	658	0.81	33.4	52.1	86.2	0.7	6.2
	658	0.09	50.7	53.9	91.7	1.5	4.3
Al-BEA	608	1.21	75.7	41.8	55.9	19.5	14.1
B-MWW	608	0.81	74.4	85.9	88.6	2.6	4.6
	658	0.85	98.6 (98.7)	86.1 (87.5)	87.6 (89.2)	3.5 (3.1)	6.6 (6.4)
	548	0.82	23.5 (23.8)	78.2 (78.8)	87.5 (87.1)	0.4 (0.5)	6.6 (8.6)
	608	0.29	39.5	79.1	91.6	1.2	4.6
	608	10.8	12.4	76.9	91.3	0.4	2.1
	608	0.31	57.5	82.6	88.3	1.6	5.3
MCM-22	608	1.20	88.1	67.7	73.9	10.4	9.4

Conversions and selectivity recorded at TOS ≈ 10h; bracketed conversions and selectivity reported at TOS≈ 48 h. Carbon balances close to within 10%. $p_{2MTHF} = 3.6$ torr. Carrier gas flowrate 35 sccm.
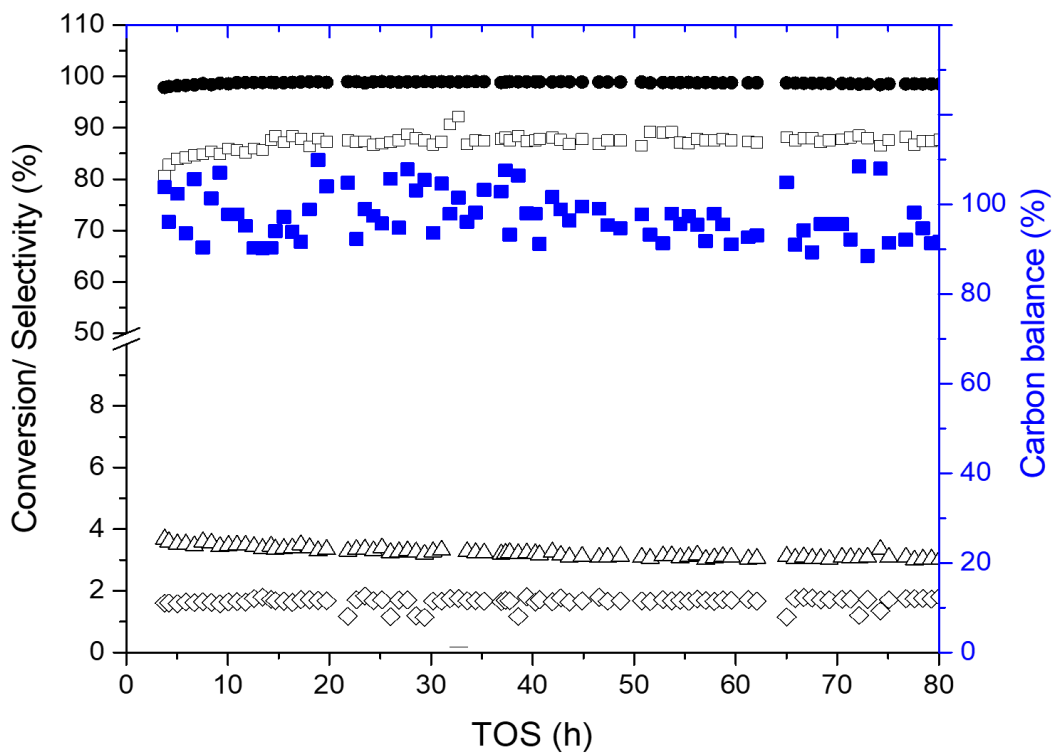
Figure S6. *(primary axis)* 2-MTHF conversion (●), and product selectivities towards 1,3-Pentadiene (□), 1,4-Pentadiene (◊), and butenes (Δ), and *(secondary axis)* Carbon mass balance (■) (Reaction conditions: T= 658 K, p_{2-MTHF} =3.6 torr, WHSV = 0.85 h^{-1}, Carrier gas flowrate= 35 sccm). Products with selectivity <2% are not shown.
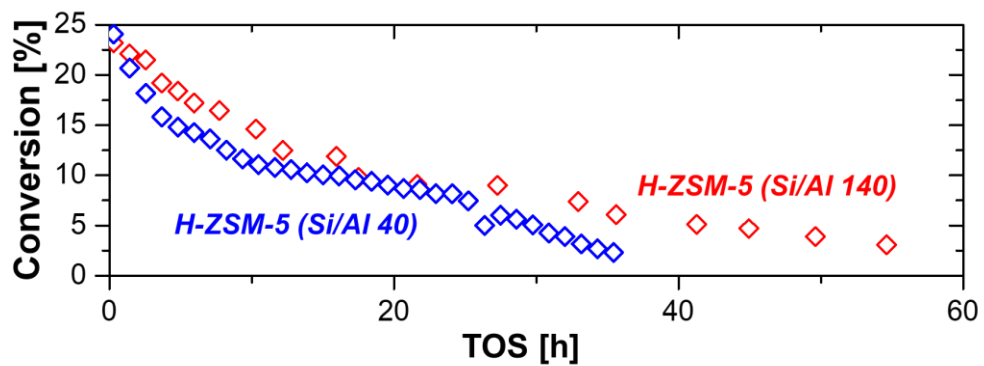
Figure S7. 2-MTHF conversion as a function of time-on-stream for aluminosilicate H-ZSM-5 with different aluminum contents (Reaction conditions: T= 658 K, P_{2-MTHF} =25 torr, WHSV = 6.8 h^{-1} for ZSM-5 (Si/Al 140), and 42.9 h^{-1} for ZSM-5 (Si/Al 40); Carrier gas flowrate= 123 sccm for ZSM-5 (Si/Al 40), and 30 sccm for ZSM-5 (Si/Al 140)).

S4. Isomerization of 1,4-Pentadiene to 1,3-Pentadiene

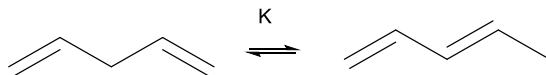### S4.1 Equilibrium calculations for the inter-conversion of 1,3-, and 1,4-Pentadiene

Table S3. Enthalpy of formation, and gas phase entropies of 1,3-PD and 1,4-PD[*] (* NIST values)

	$\Delta_f H^0$ (kJ/mol)	$S_{gas,0}$ (J/mol)
1,3-Pentadiene (E)	75.77	315.6
1,3-Pentadiene (Z)	82.72	322.8
1,4-Pentadiene	106.3	334

* Calculations are done assuming a 1:1 ratio of E:Z 1,3-PD

Table S4. Reaction enthalpies for the isomerization of 1,4-PD to 1,3-PD

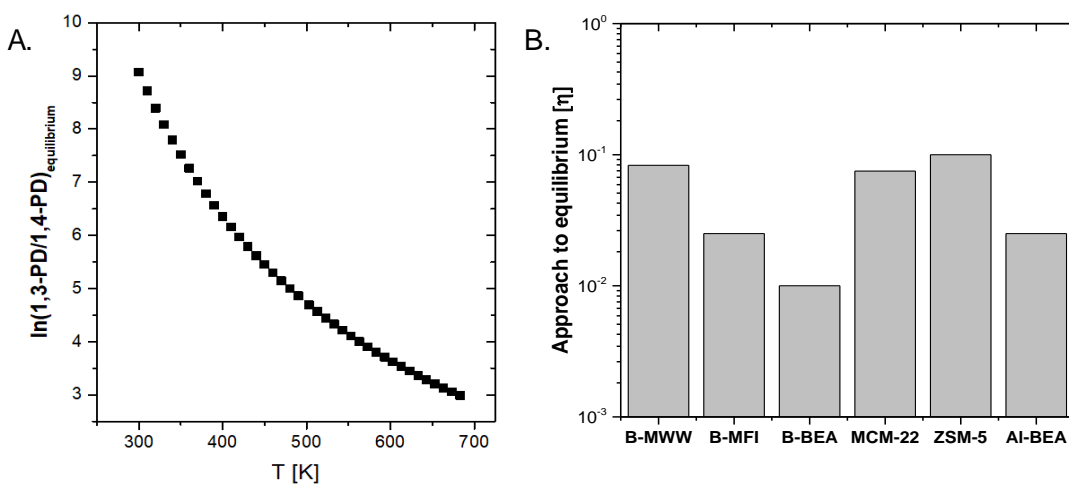|	
$\Delta_{rxn} H^0$ (kJ/mol)	-27.06
$\Delta_{rxn} S^0$ (kJ/mol)	-0.015
$\Delta_{rxn} G^0$ (kJ/mol)	-9.143
K (298 K)	9352

Figure S8. (A) Variation of the equilibrium ratio of 1,3-Pentadiene to 1,4-Pentadiene with temperature

(Van't Hoff Equation), and **(B)** The approach to equilibrium at 503 K $\left(\eta = \dfrac{\left(\frac{P_{1,3-Pentadiene}}{P_{1,4-Pentadiene}} \right)}{K_{503\ K}} \right)$ for all the

zeolites at 503 K; the plot shows that the diene distribution remains far from equilibrium on all catalysts under investigated conditions

S4.2 Catalytic evaluation of borosilicates using pure 1,3-Pentadiene, and 1,4-Pentadiene feeds
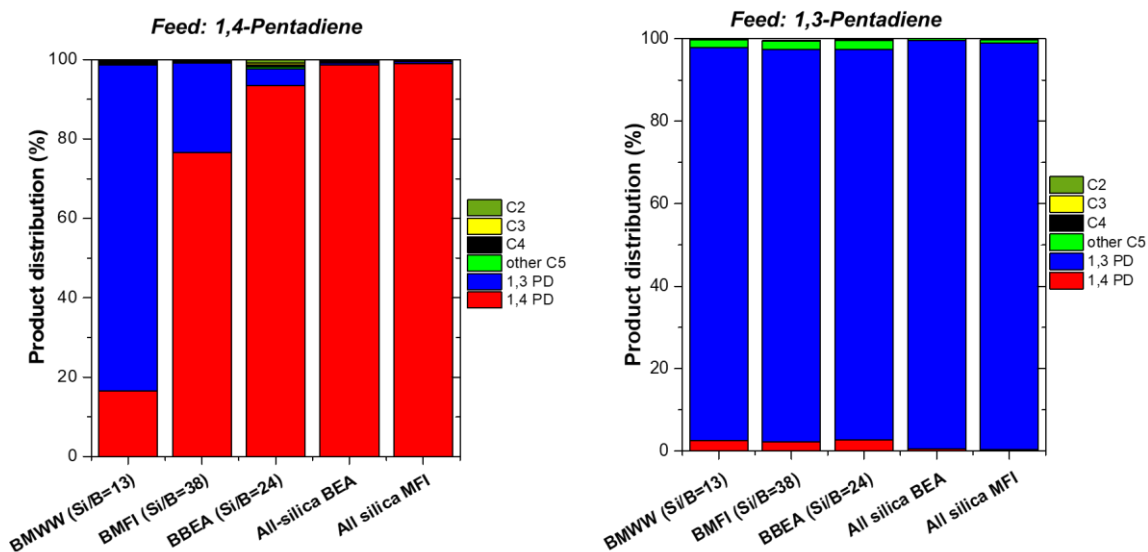

Figure S9. *(left)* Product distribution obtained using pure 1,4-Pentadiene feed on different borosilicates; *(right)* Product distribution obtained using pure 1,3-Pentadiene feed on all borosilicates (all-silica materials are added for comparison). (Reaction conditions: T= 608 K, P_{feed}=3.5 torr, WHSV = 1.5 h^{-1}, Carrier gas flowrate= 35 sccm, carbon balances close to ≈ 80-85%).

S4.3. Diene distributions resulting from pure C5 alkenol feeds on ZSM-5 (Si/Al 140)
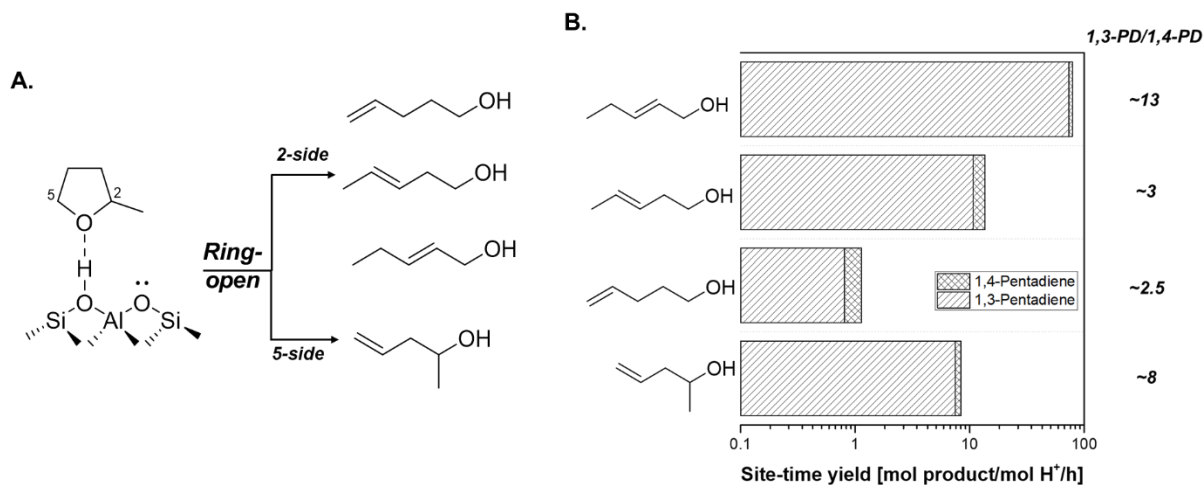

Figure S10. (A) The alkenol intermediates resulting from the ring-opening of 2-MTHF**;** and **(B)** Site time yields for the production of 1,3-Pentadiene, and 1,4-Pentadiene and the corresponding 1,3-PD/1,4-PD ratios obtained from **(top to bottom)** 2-penten-1-ol, 3-penten-1-ol, 4-penten-1-ol, and 4-penten-2-ol (Reaction conditions: T= 413 K, p_{feed}= 10.5 torr, WHSV = 3.2-6.5 h^{-1}, Carrier gas flowrate= 60 sccm, Catalyst: ZSM-5 (Zeolyst) (Si/Al=140, with a BAS count of $\approx$ 85.3 µmol/g), all conversions kept in the range 2-5%).

References

(1)   Camblor, M. a.; Corma, A.; Valencia, S. *Chem. Commun.* **1996**, 2365-2366.

(2)   M.M.J. Treacy and; Higgins, J. B. *Collection of Simulated XRD Powder Patterns for Zeolites (5th) Revised Edition*; Elsevier Science 2007, 2007; Vol. 5.

(3)   Zones, S. I.; Benin, A.; Hwang, S. J.; Xie, D.; Elomari, S.; Hsieh, M. F. *J. Am. Chem. Soc.* **2014**, *136* (4), 1462–1471.

(4)   Hwang, S. J.; Chen, C. Y.; Zones, S. I. In *Journal of Physical Chemistry B*; 2004; Vol. 108, pp 18535–18546.

(5)   Koller, H.; Fild, C.; Lobo, R. F. *Microporous Mesoporous Mater.* **2005**, *79* (1–3), 215–224.

(6)   Koller, H.; Senapati, S.; Ren, J.; Uesbeck, T.; Siozios, V.; Hunger, M.; Lobo, R. F. *J. Phys. Chem. C*, 120 (18), **2016,** 9811-9820.

(7)   Tong, H. T. T.; Koller, H. *Microporous Mesoporous Mater.* **2012**, *148* (1), 80–87.

(8)   Mihályi, R. M.; Pál-Borbély, G.; Beyer, H. K.; Szegedi, Á.; Korányi, T. I. *Microporous Mesoporous Mater.* **2007**, *98* (1–3), 132–142.

(9)   Marthala, V. R. R.; Hunger, M.; Kettner, F.; Krautscheid, H.; Chmelik, C.; Kärger, J.; Weitkamp, J. *Chem. Mater.* **2011**, *23* (10), 2521–2528.

(10)   Trudu, F.; Tabacchi, G.; Gamba, A.; Fois, E. *J. Phys. Chem. A* **2007**, *111* (45), 11626–11637.

(11)   Chen, J.; Liang, T.; Li, J.; Wang, S.; Qin, Z.; Wang, P.; Huang, L.; Fan, W.; Wang, J. *ACS Catal.* **2016**, *6* (4), 2299–2313.

(12)   Grünewald-Lüke, A.; Marier, B.; Hochgräfe, M.; Gies, H. *J. Mater. Chem.* **1999**, *9* (10), 2529–2536.

(13)   Cavalcante, C. L.; Ruthven, D. M. *Ind. Eng. Chem. Res.* **1995**, *34* (1), 185–191.